Supporting information

The catalysis of (de)lithiation in a nerve-cell-like anode of Li-ion battery

Bing Lu,[+1] Min Qu,[+1] Qian He, Zhenyang Xie, Lihan Liu, Xun Huang, Jing Li, Li Li,

Wei Ding[*], Zidong Wei[*]

Chongqing Key Laboratory of Chemical Process for Clean Energy and Resource

Utilization, School of Chemistry and Chemical Engineering, Chongqing University,

Chongqing 400044, China.

+ These authors contributed equally to this work.

[*]Corresponding authors.

E-mail address: dingwei128@cqu.edu.cn (W. D); zdwei@cqu.edu.cn (Z. Wei)

Experimental Section

1.1 Material synthesis

1.1.1 The preparation of monodisperse and hollow nanosphere SnO$_2$

All chemicals were used without further purification. In a typical experiment, the urea was dissolved in a mixed solution of 50 ml deionized water and 30 ml absolute ethyl alcohol. After complete dissolution, the potassium stannate trihydrate (K$_2$SnO$_3$·3H$_2$O, 99.9%, Aldrich) was dispersed uniformly into the above solution, stirring vigorously for 20 min. (The weight ratio of urea and K$_2$SnO$_3$·3H$_2$O is 1.28:1)

Subsequently, the mixed solution was transferred into a PTFE-lined autoclave, sealed, and kept for 20 h under 200°C. After the system cooled spontaneously to room temperature, the sediment was filtered with deionized water and absolute ethyl alcohol several times, afterwards, dried under 80°C to obtain the template-free hollow nanosphere SnO_2.

1.1.2 The preparation of hollow Sn-SnO$_2$ nanospheres encapsulated by the N-doped carbon nanofiber (SnO$_2$@NC)

The hollow nanospheres SnO_2 were stirred and dispersed uniformly in the dimethyl formamide (DMF) solution for 45 min. Subsequently, the polyacrylonitrile (PAN, $(C_3H_3N)_n$, MW = 8000, Alfa Aesar) was added to the above solution three times and stirred at 60 °C overnight. (The weight ratio of SnO_2 and PAN is 1.4:1) The as-synthesized white emulsion was sucked into a 5 ml syringe equipped with a flat-needle for electrospinning, with a working voltage of 15 kV and a feeding rate of 0.02 mm/min. Meanwhile, the distance between the Cu collector and the flat-needle was fixed at 15 cm. Whereafter, the integrated electrode of the hollow SnO_2@PAN nanosphere was carbonized to obtain the SnO_2@NC at 650 °C and Sn@NC at Ar atmosphere, 700 °C for 5h under a rising speed of 5 °C min^{-1}. The contents of the SnO_2 for SnO_2@NC was identified to be 62.1 wt% and Sn for Sn@NC was identified to be 72.2 wt% based on the Inductively Coupled Plasma mass spectrometry (ICP) results.

1.2 Material characterization

An X-ray diffractometer of Bruker AXS D8, equipped with Cu Ka radiation (λ = 0.154178 nm), was used to record X-ray diffraction (XRD) patterns and observe the

crystalline phase of the samples. A DXR Raman Microscope (Thermo Scientific) was first calibrated with a Si wafer (520 cm^{-1}) and utilized to obtain the Raman spectrum and with a laser wavelength of 532 nm. The morphology of the sample was investigated by a field emission scanning electron microscopy (FE-SEM, Helios, nanolab, 600i). Transmission electron microscopy (TEM) and element mapping images were taken on a JEOL-2100F microscope.

1.3 Electrochemical measurement

The obtained $SnO_2@NC$ and $Sn@NC$ were punched into the circular slice with a diameter of 1 cm and finally the loading mass of the active materials is typically 3.8~5.0 mg cm^{-2}. CR2025 coin cells were assembled in a glovebox with the $SnO_2@NC$ nanofiber and $Sn@NC$ electrodes, (the knife-coated electrodes are consisting of active materials, acetylene black, and PVDF binder under a weight ratio of 7:2:1, and finally the loading mass of the SnO_2 is typically 1.2~1.5 mg cm^{-2}) the lithium foil as the counter electrode, the porous polypropylene-based membrane (Celgard) as the separator, and 1 mol L^{-1} LiPF$_6$ insolvent of ethylene carbonate (EC): dimethyl carbonate (DMC)=1:1 as the electrolyte in an argon atmosphere. The oxygen and water contents in the glove box were both less than 0.1 ppm. The high loading of 3.8-5 mg cm^{-2} can be easily achieved in the designed nerve-cell-like electrodes due to the well connection of active materials. In the traditional knife-coating process, however, the high loading of 3.8-5 mg cm^{-2} would lead to the collapse of the electrode structure, and eventually, lead to poor battery performance. After careful optimization, the loading of ~1.5 mg cm^{-2} was adopted in the blank SnO_2 electrode with the highest battery performance for

comparison.

The theoretical Li-storage capacity is 1068.8 mAh g^{-1} and 820.6 mAh g^{-1} in the SnO$_2$@NC and Sn@NC, respectively. Galvanostatic charge-discharge tests were performed in the voltage range of 0.01–2.5 V vs. Li$^+$/Li using the Land battery test system. Cyclic voltammetry (CV) was carried out on CHI 660e with a scan rate of 0.1 mV s^{-1}. Electrochemical impedance spectroscopy (EIS) tests were performed in the frequency range from 100 kHz to 100 mHz on the Versa STAT 4 under 5 mV s^{-1}. The specific capacities were calculated based on the total mass of the nerve cell-like SnO$_2$@NC and Sn@NC respectively. Note: The test current density of 1 C was set at 160 mA g^{-1} in the full cell test.
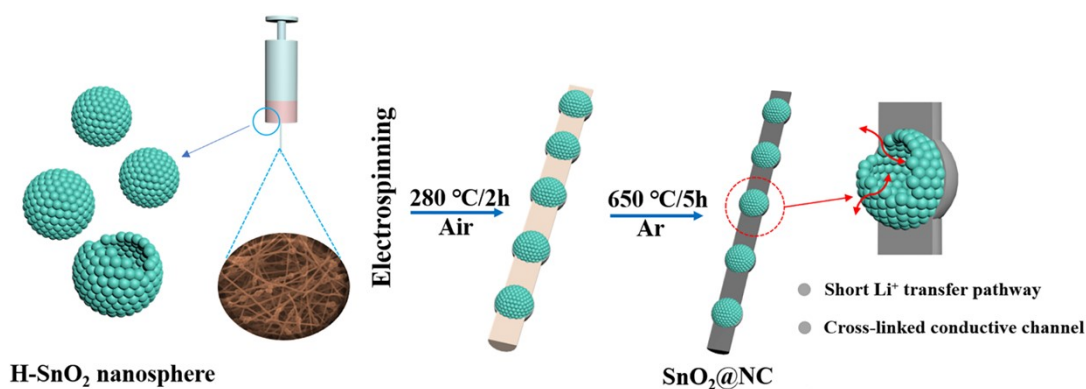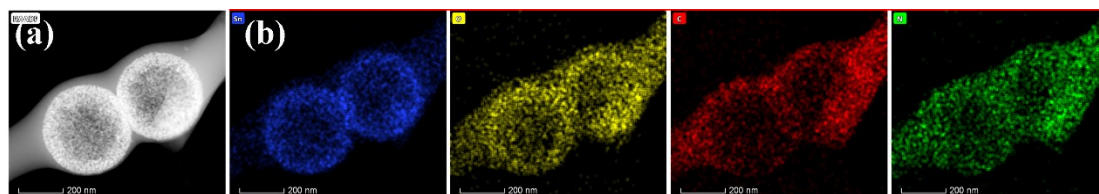

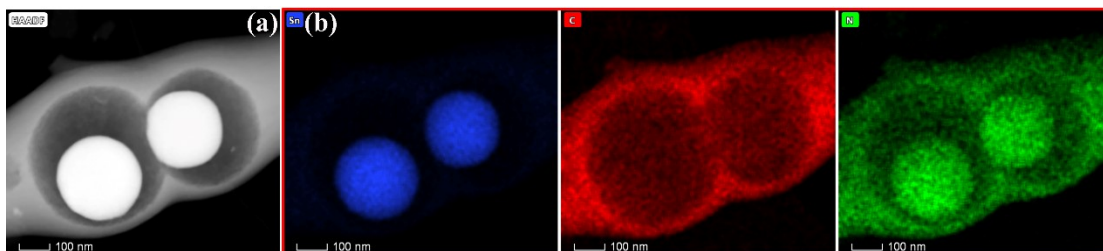**Figure S1.** The schematic illustration of the preparation strategy of the nerve cell-like SnO$_2$@NC.
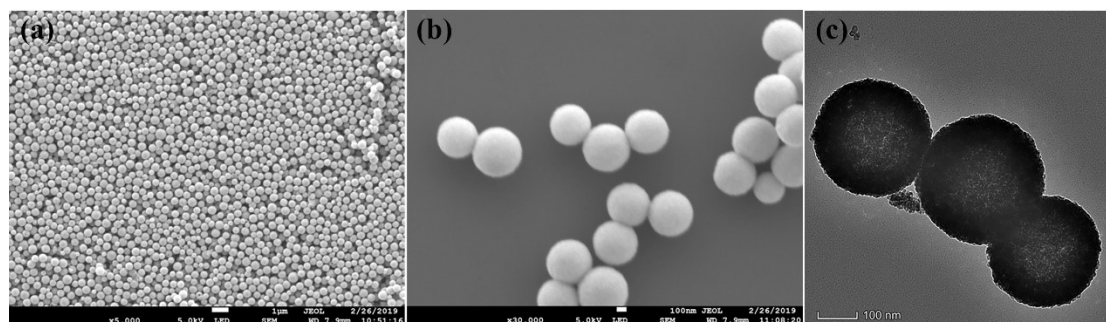
Figure S2. The SEM images of the SnO$_2$ (a-b) and TEM image of the SnO$_2$ (c).
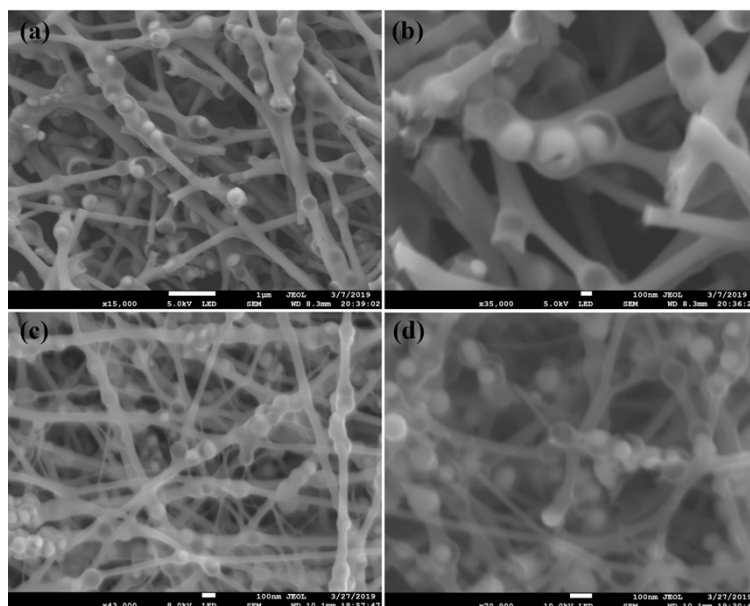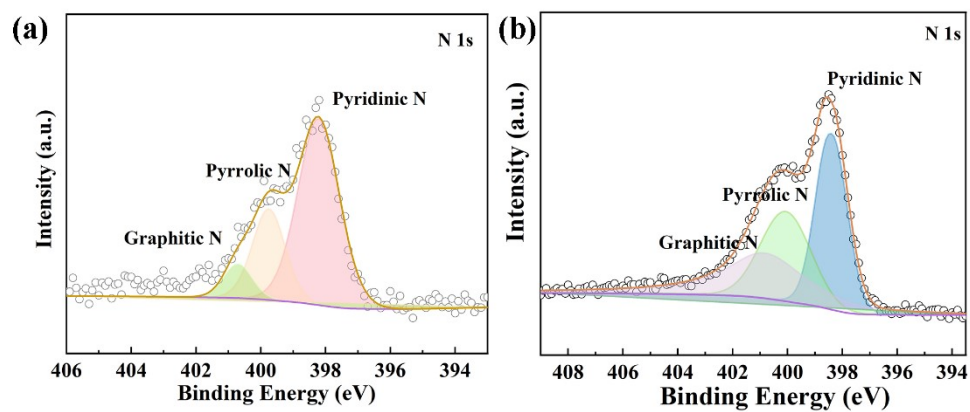
Figure S3. The SEM images of the nerve cell-like Sn@NC (a-b) under 700°C, 800°C (c), and 900°C (d).

Figure S4. The STEM image (a) and (b) elemental mapping images for the corresponding SnO$_2$@NC indicating the existence of Sn, O, C, N.
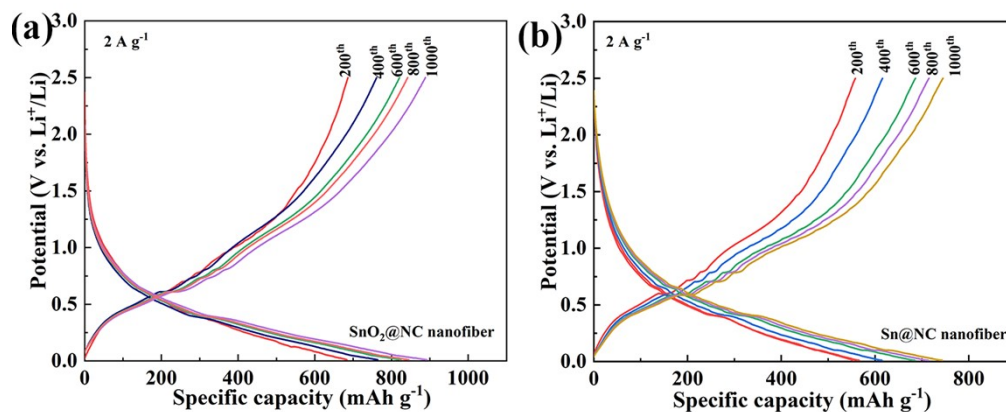

Figure S5. The STEM image (a) and (b) elemental mapping images for the corresponding Sn@NC indicating the existence of Sn, C, N.
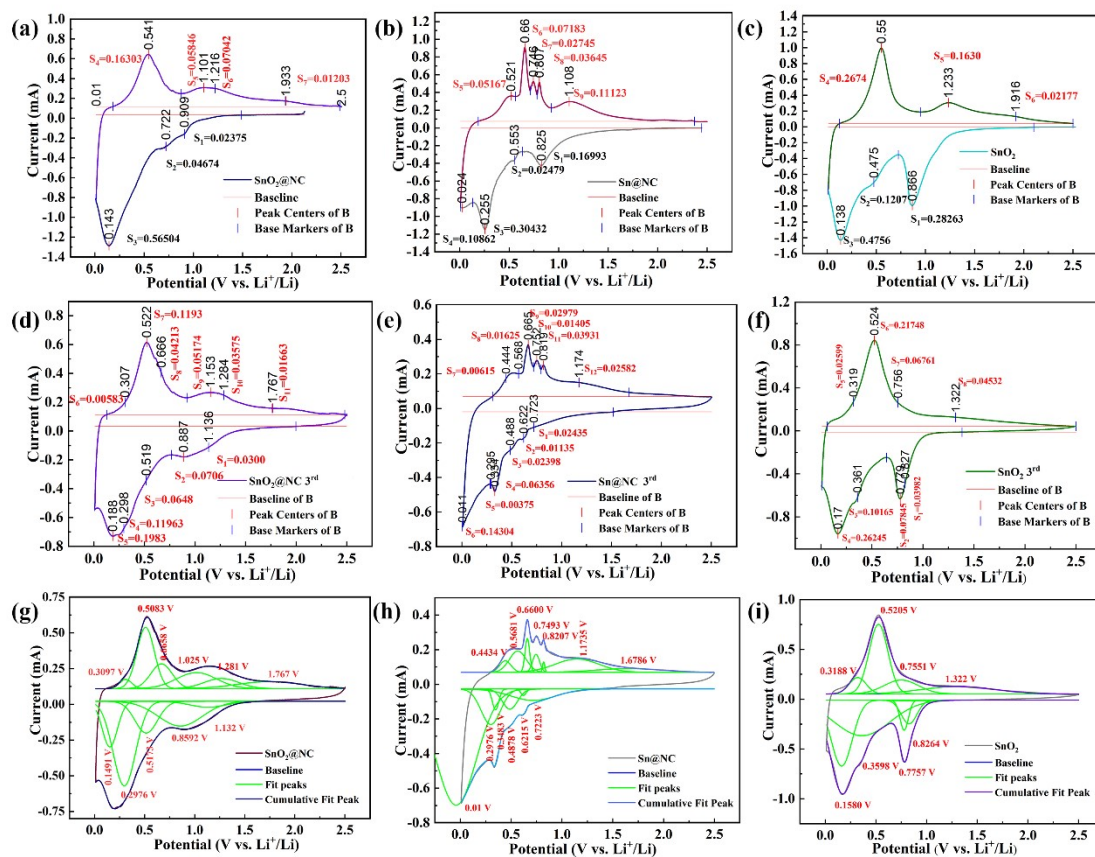

Figure S6. The high-resolution XPS spectra of the SnO$_2$@NC and Sn@NC for the corresponding
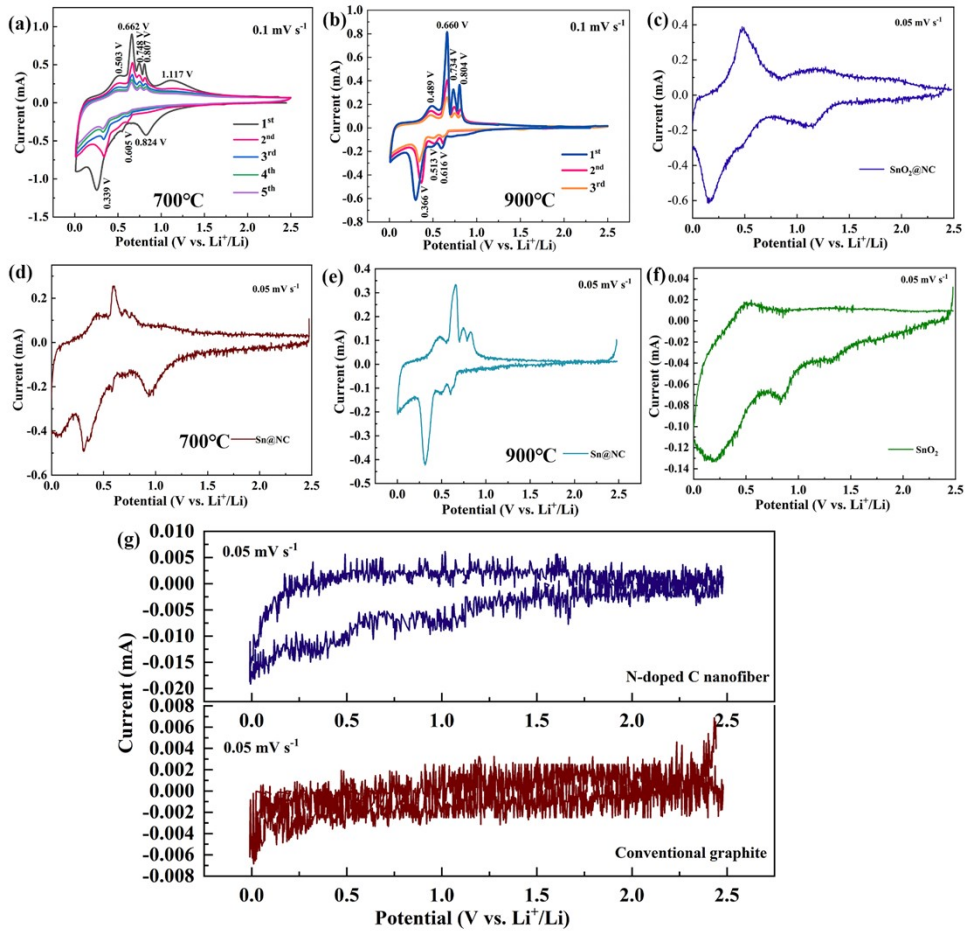
Gaussian fitting of N 1s.

Figure S7. The GCD curves of $SnO_2@NC$ (a) and (b) $Sn@NC$ under 2 A g^{-1} at 0.01-2.5 V (Vs Li^+/Li).

Figure S8. The integration of the 1st CV curves for $SnO_2@NC$ (a), $Sn@NC$ (b), and SnO_2 (c) under 0.1 mV s^{-1} at working voltage range of 0.01-2.5 V (Vs Li^+/Li); the integration of the 3rd CV curves for $SnO_2@NC$ (d), $Sn@NC$ (e), and SnO_2 (f); the deconvoluted peaks in the 3rd cycle for $SnO_2@NC$ (g), $Sn@NC$ (h), and SnO_2 (i).

Figure S9. The CV curves for Sn@NC-700℃ (a), and (b) Sn@NC-900℃ under 0.1 mV s^{-1} at working voltage range of 0.01-2.5 V (Vs Li$^+$/Li) in coin cells; the three-electrode catalytic tests for the SnO$_2$@NC (c), the Sn@NC at 700℃ (d)-900℃ (e), and SnO$_2$ (f) under 0.05 mV s^{-1}. (The SnO$_2$@NC, the Sn@NC, or SnO$_2$ used as working electrodes; the lithium foil is used as reference and counter electrodes respectively); (g) the three-electrode tests of N-doped C nanofiber and graphite under 0.05 mV s^{-1}. (The N-doped C nanofiber or the graphite used as a working electrode; the lithium foil used as reference and counter electrodes respectively)
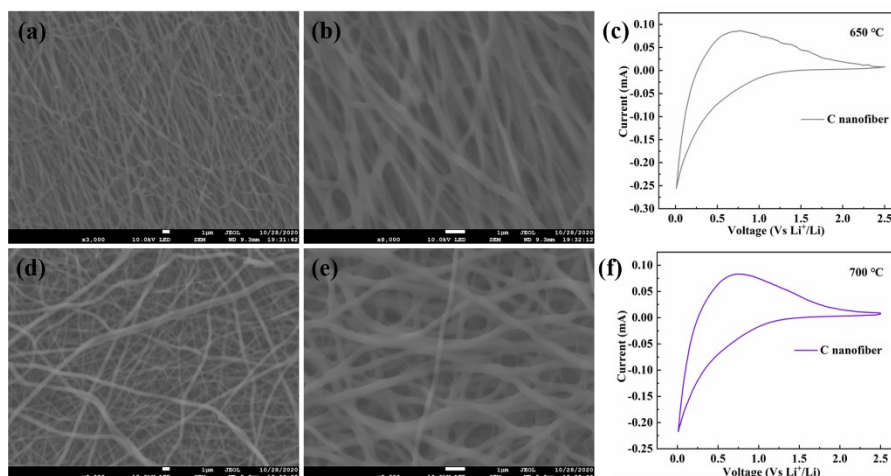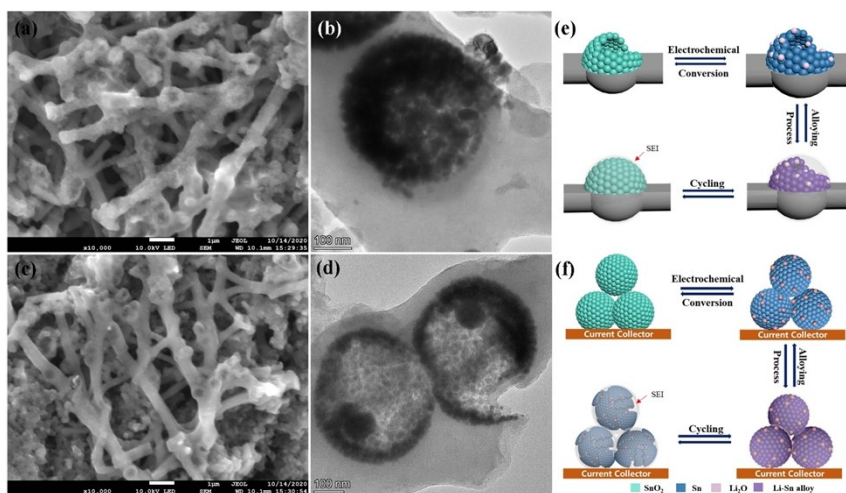

Figure S10. The SEM images of the carbon nanofiber at 650℃ (a-b) and at 700℃ (d-e); the corresponding CV curves at 650 ℃ (c) and at 700 ℃ (f) under 0.1 mV s^{-1} of voltage range 0.01-2.5 V

(Vs Li+/Li).
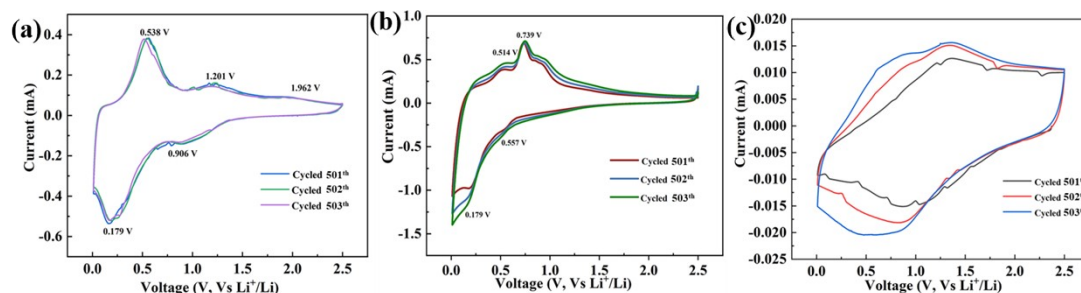

Figure S11. The CV curves under 0.1 mV s^{-1} of SnO$_2$@NC at 650 °C (a), Sn@NC-700 °C (b), blank sample SnO$_2$ nanosphere (c) after 500 cycles at 2 A g^{-1}.

Figure S12. (a) The SEM and (b) TEM images of SnO$_2$@NC, and the SEM image (c) and TEM (d) of Sn@NC after 1000 cycles at 2 A g^{-1}; Representation of the structural evolution of the (e) the nerve cell-like SnO$_2$@NC and Sn@NC, and (f) traditional SnO$_2$ electrode upon a discharge and charge cycle.
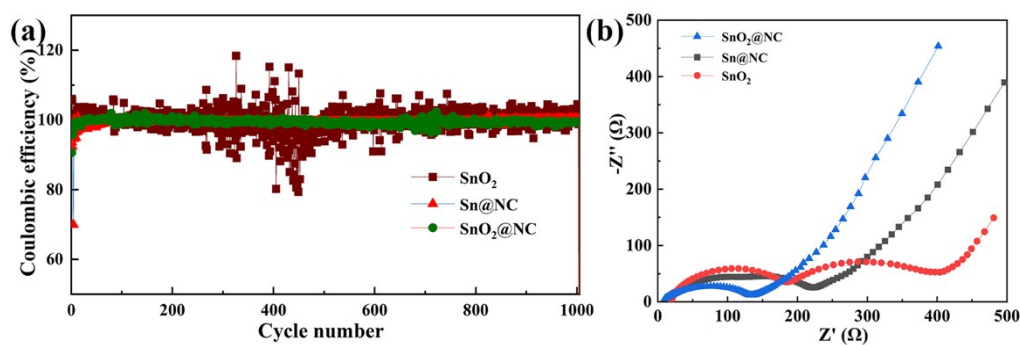
Figure S13. The coulombic efficiency for SnO$_2$@NC (a), Sn@NC, and SnO$_2$ under 2 A g^{-1} at working voltage range of 0.01-2.5 V (Vs Li+/Li); (b) the EIS after 1000 cycles of SnO$_2$@NC, Sn@NC, and SnO$_2$ electrodes.
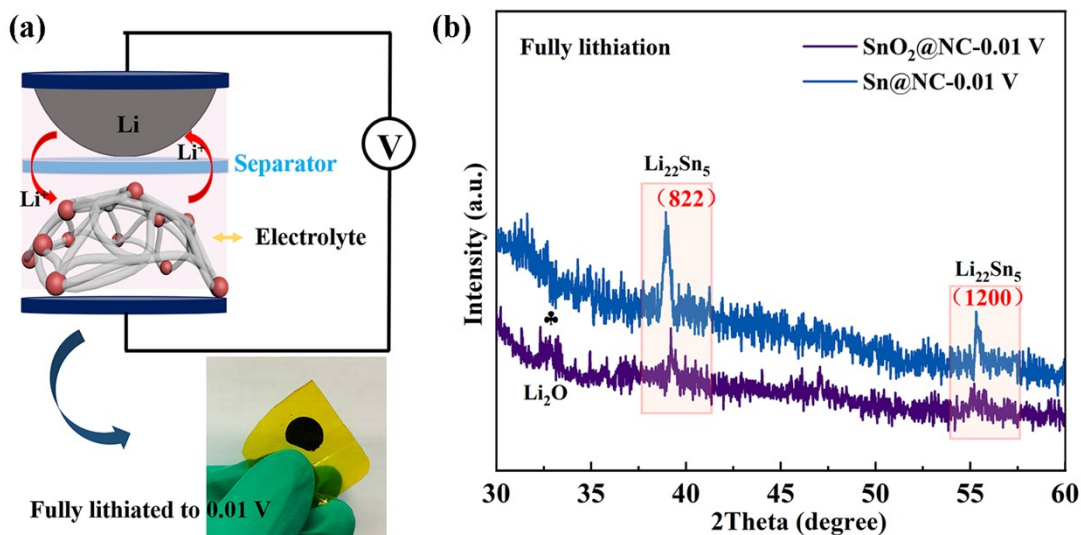
Figure S14. (a) The preparation of ex-situ electrodes under fully lithiation state and (b) the ex-situ XRD results of SnO$_2$@NC and Sn@NC electrodes.

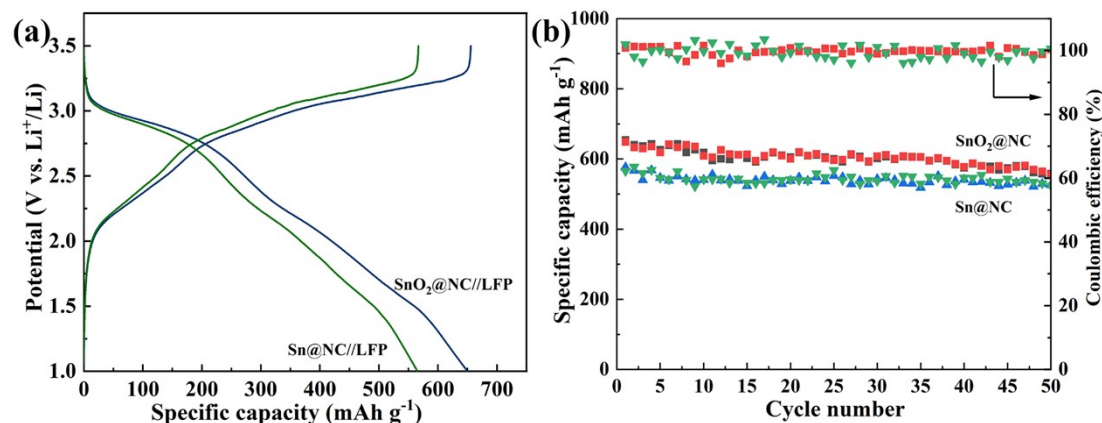**Figure S15.** (a) The GCD curves of SnO$_2$@NC//LFP and Sn@NC//LFP under 0.05C; (b) the cycling performance of SnO$_2$@NC//LFP and Sn@NC//LFP under 0.2 C at 1.0-3.5 V (vs Li$^+$/Li).
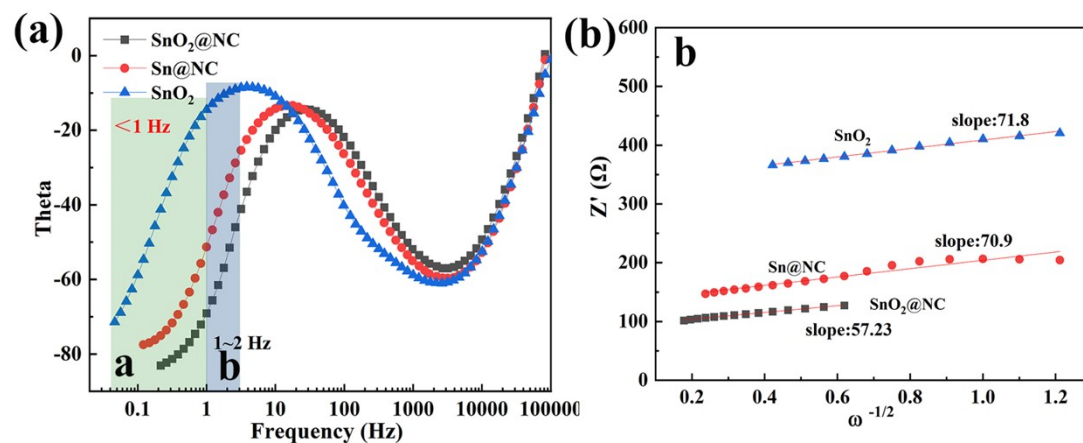
Figure S16 (a) The theta-frequency analysis of the three electrodes; (b) the fitting lines for the real part of the complex impedance versus $\omega_{-1/2}$ at 25 °C: the selected frequency in the #b region.

Table S1. The potentials under integration peaks of coverage 0.5 for the dealloying process and

electrochemical conversion (EC) in the three electrodes.

Cycle number	SnO$_2$@NC		Sn@NC		SnO$_2$	
	Dealloying	EC	Dealloying	EC	Dealloying	EC
1st	0.556 V	1.043 V / 1.272 V	0.659 V	1.128 V	0.553 V	1.224 V / 1.169 V
3rd	0.556 V	1.025 V / 1.281 V	0.684 V	1.174 V	0.535 V	1.332 V

Table S2. The corresponding loading mass of the three electrodes.

Loading mass (mg cm^{-2})	SnO$_2$@NC-cell	Sn@NC-cell	SnO$_2$-cell
Active material	3.8~5.0	3.8~5.0	~1.2
Acetylene black	0	0	~0.343
PVDF	0	0	~0.17

Table S3. Comparison of this work with recently reported SnO$_2$-based anode materials.

Samples	Initial CE	Current density (A g^{-1})	Capacity (mAh g^{-1})	Cycle number	Ref.
SnO$_2$/GeO$_2$IO	70.9%(0.1 A g^{-1})	0.45	431	750	[1]
SnO$_2$@HPC@NC	75.2%(0.1 A g^{-1})	1.0	767	500	[2]
c-SnO$_2$@3D-CNT	72.2%(0.05 A g^{-1})	1.0	452.0	1000	[3]
H-TiO$_2$@SnS$_2$@PPy	71.2%(0.2 A g^{-1})	2.0	508.7	2000	[4]
SnO$_2$/CNT	62.5%(0.05 A g^{-1})	0.1	546	100	[5]
Porous SnO$_{2-\delta}$@NC	74.3%(0.1 A g^{-1})	1.0	543	1000	[6]
NSGS-8	60.1%(0.1 A g^{-1})	2.0	480.2	2000	[7]
Sn/SnO$_2$@C	57.2%(0.2 A g^{-1})	1	986.3	2000	[8]
SnO$_2$@NC	86.5%(0.05 A g^{-1})	2.0	842.3	1000	In this work
		7.0	691.94	-	

Table S4. Impedance indexes simulated from the equivalent circuits for the EIS of SnO$_2$@NC and Sn@NC under fully lithiation state (0.01 V) in three-electrode system.

Sample	Potential (V)	R$_e$	R$_{sei}$	R$_{ct}$
SnO$_2$@NC	0.01 V	8.019 Ω	R$_{Li2O}$:17.65 Ω	24.23 Ω
Sn@NC	0.01 V	7.49 Ω	R$_{sei}$:1.557 Ω	46.06 Ω

Computational details

Calculations were performed using the Vienna ab initio Simulation Package (VASP). Electron-ion interactions were described by the projector augmented wave (PAW) pseudopotentials provided in the VASP database. The Perdew–Burke–

Ernzerhof (PBE) functional within the generalized gradient approximation (GGA) was used to implement DFT calculations. The energy cut-off for the plane-wave basis expansion was chosen to be 400 eV. A conjugate-gradient algorithm was employed to relax the ions into their instantaneous ground state. Gaussian smearing with a width of 0.05 eV was also utilized. For the surface Brillouin zone integration, a $3\times3\times1$ Monkhorst-Pack k-point mesh was used. Geometric optimizations were pursued until the force on each atom fell below the convergence criterion of 0.02 eV·Å^{-1} and the energy converged within 10^{-5} eV, respectively.

Four layered Sn (101) slabs and $Li_{22}Sn_5$ (822) slabs were employed to model the composite structure with Li_2O cluster (Li_xO_y), labeled as Sn-Li_2O, and Sn_5Li_{22}-Li_2O respectively. The bottom two layers of the slabs are fixed to resemble bulk behavior. A vacuum layer of ~15 Å was added above the metal surface in the Z direction to avoid any interaction between planes. The adsorption energies (ΔE_{ads}) of Li atom on Sn(101) and Sn-Li_2O surface, and Li vacancy formation energy （E_{vac}） on $Li_{22}Sn_5$ (822) and $Li_{22}Sn_5$-Li_2O surface is determined by Equation (1) and Equation (2) respectively:

$$\Delta Eads = Eads/base - Eads - Ebase \qquad （1）$$

$$Ef^{vac} = Erel^{vac}(n-1,v') = Ec - Erel(n,v) \qquad （2）$$

In Eq. (1), where $Eads/base$, $Eads$ and $Ebase$ are the total energy of the adsorbed systems, the Li atoms, and base materials (Sn or Sn-Li_2O), respectively. Accordingly, a negative $\Delta Eads$ indicated spontaneous adsorption between the adsorbate and base materials. In Eq. (2), E_{rel}^{vac}, $E_{rel,}$ and E_c are the total energy of a vacant protocell, the total energy of a non-vacant protocell, and the energy of an independent atom

respectively. where n, v, and v' are respectively the total number of lattice points, the volume of the complete cell, and the volume of the cell with a vacancy. From the perspective of thermodynamics, more negative vacancy formation energy indicates that the lithium removal process is more likely to occur.
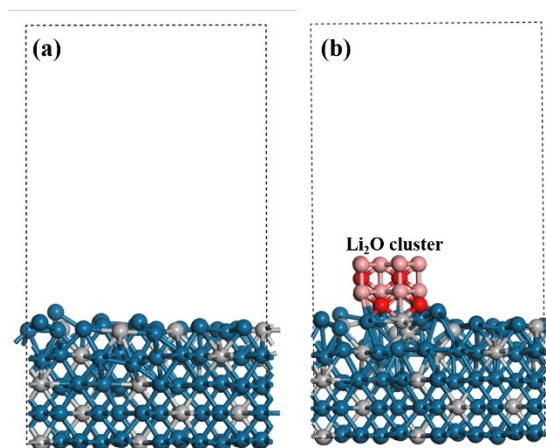
Figure S17. The side view of the $Li_{22}Sn_5$ (822) (a) and $Li_{22}Sn_5$ (822)-Li_2O (b) models; the insert is the Li_2O cluster.
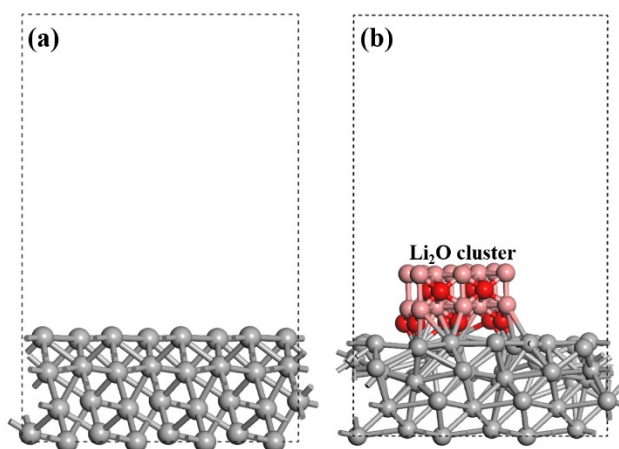
Figure S18. The side view of the Sn (101) (a) and Sn (101)-Li_2O (b) models; the insert is the Li_2O cluster.
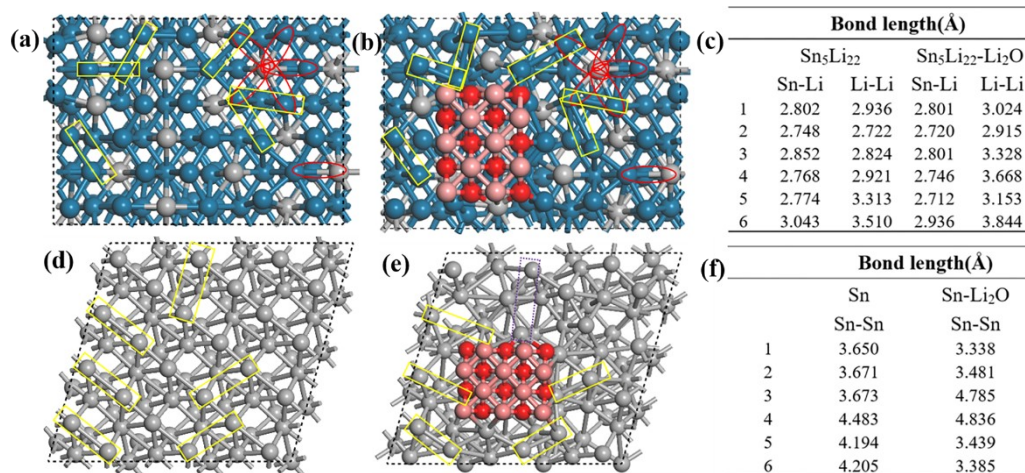
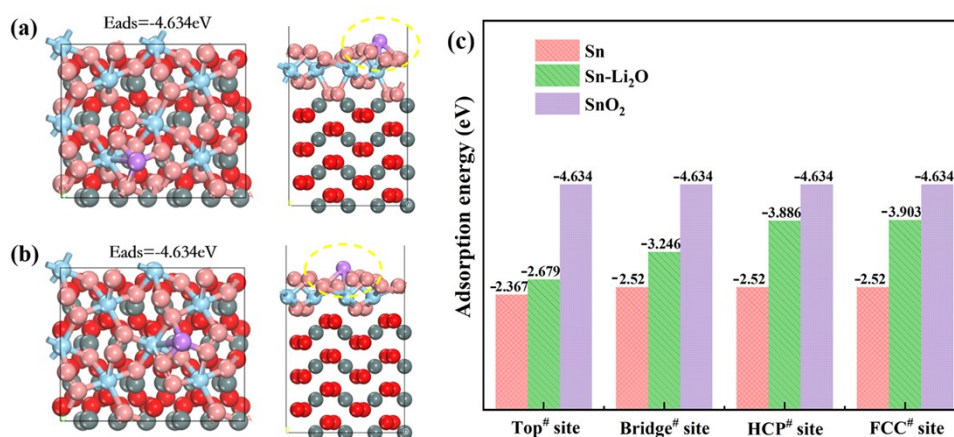**Figure S19.** The bond length of Li-Li bond on (a) $Li_{22}Sn_5$ (822) and (b) $Li_{22}Sn_5$ (822)-Li_2O surface (The rectangular boxes represent the Li-Li bond and the ellipses represent the Sn-Li bond), and Table (c): the corresponding bond length data (Clockwise); Bond length of Li-Li bond on (d) Sn (101) and (e) Sn (101)-Li_2O surface (the rectangular boxes represent the Sn-Sn bond), and Table (f): the corresponding bond length data (Clockwise).

The bond length tables in the figure:

	Bond length(Å)			
	Sn_5Li_{22}		Sn_5Li_{22}-Li_2O	
	Sn-Li	Li-Li	Sn-Li	Li-Li
1	2.802	2.936	2.801	3.024
2	2.748	2.722	2.720	2.915
3	2.852	2.824	2.801	3.328
4	2.768	2.921	2.746	3.668
5	2.774	3.313	2.712	3.153
6	3.043	3.510	2.936	3.844

	Bond length(Å)	
	Sn	Sn-Li_2O
	Sn-Sn	Sn-Sn
1	3.650	3.338
2	3.671	3.481
3	3.673	4.785
4	4.483	4.836
5	4.194	3.439
6	4.205	3.385

Figure S20. Adsorption energy of lithium atom at different sites of SnO_2 (101) (a) top site and (b) bridge site; (The first layer: the purple is lithium, the light blue is tin and the pink is oxygen; the below layer: the red is oxygen and the grey is tin) (c) the Li adsorption energy of SnO_2, Sn, and Sn/Li_2O.

Reference

1. D. McNulty, H. Geaney, Q. Ramasse and C. O'Dwyer, *Advanced Functional Materials*, 2020, DOI: 10.1002/adfm.202005073, 2005073.
2. Y. Hong, W. Mao, Q. Hu, S. Chang, D. Li, J. Zhang, G. Liu and G. Ai, *Journal of Power Sources*, 2019, **428**, 44-52.
3. P. Bhattacharya, J. H. Lee, K. K. Kar and H. S. Park, *Chemical Engineering Journal*, 2019, **369**, 422-431.
4. L. Wu, J. Zheng, L. Wang, X. Xiong, Y. Shao, G. Wang, J. H. Wang, S. Zhong and M. Wu, *Angew Chem Int Ed Engl*, 2019, **58**, 811-815.
5. Y. Cheng, J. Huang, H. Qi, L. Cao, J. Yang, Q. Xi, X. Luo, K. Yanagisawa and J. Li, *Small*, 2017, **13**.
6. R. Jia, J. Yue, Q. Xia, J. Xu, X. Zhu, S. Sun, T. Zhai and H. Xia, *Energy Storage Materials*, 2018, **13**, 303-311.
7. H.-g. Wang, Q. Wu, Y. Wang, X. Wang, L. Wu, S. Song and H. Zhang, *Advanced Energy Materials*, 2019, **9**, 1802993.
8. S. Gao, N. Wang, S. Li, D. Li, Z. Cui, G. Yue, J. Liu, X. Zhao, L. Jiang and Y. Zhao, *Angew Chem Int Ed Engl*, 2020, **59**, 2465-2472.